ELSEVIER

Physica D 124 (1998) 177–200

PHYSICA D

Tongue-like bifurcation structures of the mean-field dynamics in a network of chaotic elements

Tatsuo Shibata *, Kunihiko Kaneko [1]

Department of Pure and Applied Sciences, University of Tokyo, Komaba, Meguro-ku, Tokyo 153-8902, Japan

Received 19 February 1998; received in revised form 2 June 1998; accepted 16 June 1998
Communicated by Y. Kuramoto

Abstract

Collective behavior is studied in globally coupled maps. Several coherent motions exist, even in fully desynchronized state. To characterize the collective behavior, we introduce scaling transformation of parameters, and detect in parameter space a tongue-like structure in which collective motion is possible. Such a collective motion is supported by the separation of timescales, given by the self-consistent relationship between the collective motion and chaotic dynamics of each element. It is shown that the change of collective motion is related with the window structure of a single one-dimensional map. Formation and collapse of regular collective motion are understood as the internal bifurcation structure. Coexistence of multiple attractors with different collective behaviors is also found in fully desynchronized state. © 1998 Elsevier Science B.V.

PACS: 05.45+b; 05.90+m; 87.10+e
Keywords: Globally coupled map; Collective motion

1. Introduction

Whereas the research of low-dimensional chaos provided us with important notion of unpredictability in deterministic systems, it was soon realized that many natural systems show much more complicated behavior than low-dimensional chaos. One of the important features in natural systems is high-dimensionality. Although deterministic aspects remain in the high-dimensional chaos, the present nonlinear dynamics tools are not sufficient to distinguish it clearly from noise. Hence, the study of high-dimensional chaos is important both from a theoretical and from a practical point of view.

Globally coupled dynamical systems, consisting of many dynamical elements interacting all-to-all, are good examples using which we can develop notions in high-dimensional systems. This class of dynamical systems is seen in physical, chemical and biological systems. In physics, coupled Josephson junction arrays [1] are a coupled nonlinear oscillator circuit with global feedback. In nonlinear optics with multi-mode excitation [2] many modes are often coupled globally through energy currency. In bioscience and medical science, neural [3], cellular [4], and vital [5] organizations, that are known to exhibit complex chaotic behaviors, are described in terms of a network of active elements. Several examples in ecological and

* Corresponding author. E-mail: shibata@complex.c.u-tokyo.ac.jp
[1] E-mail: kaneko@cyber.c.u-tokyo.ac.jp

PII: S0167-2789(98)00190-0

economic systems are also seen in terms of a network of active agents. Among these complex networks, a globally coupled dynamical system is the simplest case.

So far, study of globally coupled dynamical systems has revealed novel concepts [6] such as clustering, chaotic itinerancy, and partial ordering. In particular, the study of collective dynamics has got much attention [7–21]. When the interactions between elements are small enough, each element oscillates independently, without synchronization between them. Thus the number of degrees of freedom of the system is effectively proportional to the system size. If each element has chaotic dynamics, the system is in a high-dimensional chaotic state. Even in such a case, a macroscopic variable shows some kind of complicated dynamics rather than noise, ranging from low-dimensional torus to high-dimensional chaos [12,18]. This may imply that any weak interaction between active elements necessarily brings about some sort of correlation [2] between the elements.

The purpose of the present paper is to study the nature of such collective motion, using a globally coupled map [6], and to present a mechanism for the origin of such collective dynamics. With the change of the control parameters, the collective dynamics shows some sort of bifurcation. We present how elements are organized to show the bifurcation structure in the collective dynamics.

In Section 2, the globally coupled logistic map is introduced and its characteristic behavior is presented as a brief review. In Section 3, an overview of different kinds of collective dynamics is presented. In the macroscopic dynamics, a lower dimensional motion and a much longer timescale than those of microscopic dynamics are observed.

We focus on the thermodynamic limit of such collective behavior. In Section 4, the timescale and the amplitude of collective motion are studied in the large system size limit. In Section 5, a global phase diagram in the parameter space is presented. Because the phase diagram shows a complicated structure, we introduce a scaled nonlinearity parameter so that tongue-like bifurcation structures are clarified. Collective dynamics with a larger amplitude exists in each tongue structure that corresponds to a periodic window in the single logistic map. The elements are accumulated to few bands corresponding to the window of the single logistic map for a small coupling. Since windows of the single logistic map exist in any neighborhood in the parameter space, the clarification of the collective dynamics with such bands is necessary to understand the collective dynamics in general. Thus we focus on such tongue structures in Section 6, to reveal a mechanism of collective dynamics, where internal bifurcation of elements plays a key role. In Section 7, the bifurcation of the tongue structure is studied in connection with the internal bifurcation. Even within the same tongue structure, we can observe different types of collective motion. A scaling relation between the growth of tongue structure and the coupling strength is given in Section 8. In Section 9, hysteresis and multiple attractor phenomena of the collective motion are reported. This paper ends in Section 10 with summary and discussion.

2. A simple network model of chaotic elements on globally coupled map

In the present paper the following globally coupled map (GCM) is studied:

$$x_{n+1}(i) = (1-\epsilon) f(x_n(i)) + \frac{\epsilon}{N} \sum_{j=1}^{N} f(x_n(j)) \quad (i = 1, 2, 3, \ldots, N), \tag{1}$$

where $x_n(i)$ is the variable of the ith element at discrete time step n, and $f(x)$ is the internal dynamics of each element. For the internal dynamics we choose the logistic map

$$f(x) = 1 - ax^2, \tag{2}$$

where a is the nonlinearity parameter. The nonlinearity parameter a, the coupling strength ϵ, and the total number of elements N are the control parameters of the GCM.

[2] This means that two point mutual correlation does not vanish in the limit of $N \to \infty$.

The GCM can be considered as a mean-field extension of the coupled map lattice (CML) [22], in which elements are located at discrete spatial coordinates and interact with their neighbors. A GCM can be also considered as a CML in which the number of spatial dimensions goes to infinity.

In the GCM model, two opposite tendencies coexist: all-to-all coupling tends to synchronize elements, while chaotic instability in each element tends to desynchronize them. Depending on the balance between these two tendencies, a rich variety of phenomena has been found [6].

If the coupling strength ϵ is small enough, none of the elements take the same values, and the correlation between elements gets smaller [7,8] (called *desynchronized phase*). In this case, in general, all Lyapunov exponents are positive and the number of degrees of freedom in the system is proportional to the system size N. In the desynchronized state, the mean-field is not stationary, and a kind of collective dynamics is observed. In this paper we focus on the macroscopic state of this desynchronized state. The macroscopic state is characterized by the dynamics and statistics of the mean-field

$$h_n = \frac{1}{N}\sum_{j=1}^{N} f(x_n(j)). \tag{3}$$

In the next section, we will show some phenomena of macroscopic dynamics in the desynchronized state.

3. Phenomenology of collective motion in desynchronized state

Since there is no mutual synchronization among elements, one might imagine that the mean-field would be effectively the same as noise and, therefore the mean-field would go to a constant with the increase of N. One might expect that such a high-dimensional dynamics is not distinguishable from noise.

In fact this is not the case. One of the authors has found that the mean-field dynamics is different from noise, and studied its nature as "hidden coherence" [7,8]. A possible simple solution to such collective dynamics is the low-dimensional mean-field dynamics in the thermodynamic limit ($N \to \infty$), even though each element is chaotic and mutually desynchronized. Such examples have been found recently in short-ranged CML and cellular automata [10], globally coupled oscillators [23,24], the globally coupled tent map [12,16,20,21], and a globally coupled logistic map with heterogeneous elements [18].

In the present case, the collective dynamics is not given by such low dimensional dynamics [8], although it has some structure distinguishable from noise. Let us give a few sets of examples of the mean-field dynamics.

Fig. 1(a) shows an example of the time series of the mean-field as a function of time step n at every two steps, and the corresponding return map of the mean-field for $N = 10^5$. The coupling strength is too small to synchronize any two elements. The trajectory of the mean-field has some fluctuation due to the finite system size. With the increase of the system size to $N = 10^7$, however, the trajectory shows some coherent motion as is shown in Fig. 1(b). The trajectory is rather close to quasiperiodic motion, although the points are scattered around the "torus" motion. In Fig. 2, power spectra for the time series of a single element and for the mean-field are shown. The timescale of the mean-field dynamics is much longer than the timescale of the single element dynamics.

Note that the width around the closed curve remains finite when N is further increased. The collective dynamics is not on a two-dimensional torus, and it indeed is not represented by low-dimensional dynamics as will be demonstrated in Section 4. On the other hand, since the mean-field dynamics does not approach a point with the increase of N, it is also different from noise. Hence the collective motion has some structure, although it is high-dimensional.

Another set of examples is given in Fig. 3, which are the time series plotted at every seven steps and the first return maps. In Fig. 3(a), quasiperiodic-like motion is not detected in the mean-field dynamics, but some structure exists in the return map, whereas in the time series, a characteristic timescale seems to exist. With a slight increase of a, the dynamics of the mean-field is changed as in Fig. 3(b). In this case, the return map does not show a clear structure, and the variation of

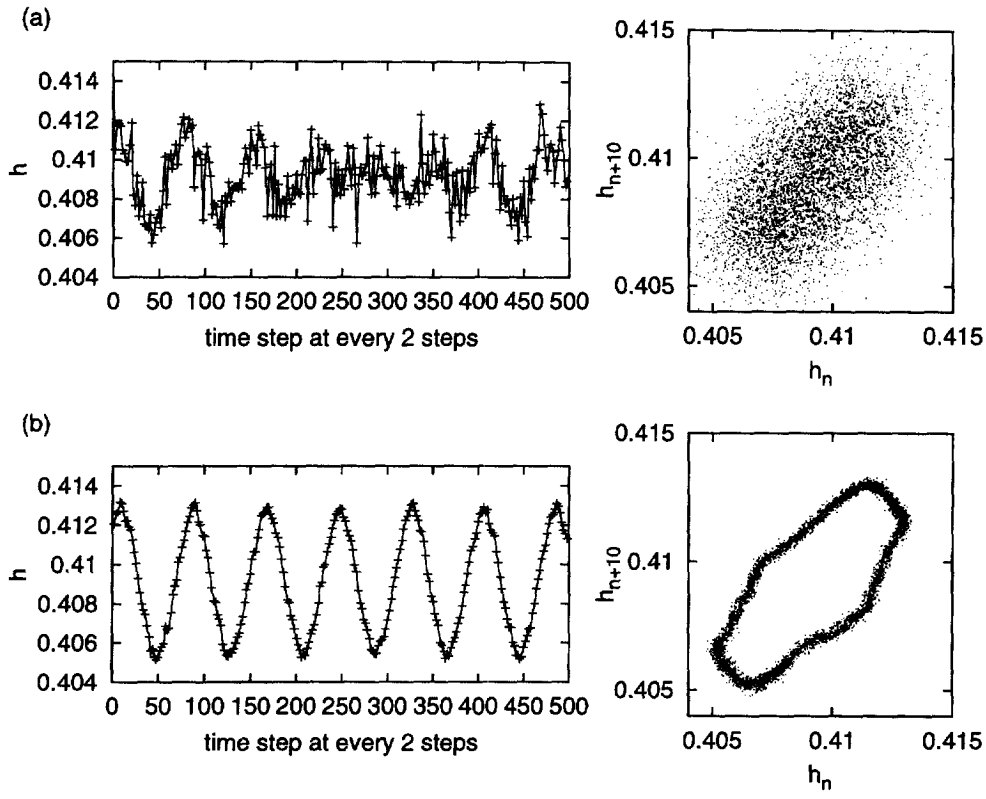

Fig. 1. Time series and return map. Time series are plotted at every two steps after transients are discarded. $a = 1.5449205$, $\epsilon = 0.0005$. (a) $N = 10^5$, (b) $N = 10^7$. Corresponding return maps (h_n, h_{n+10}) are plotted over 50 000 steps after transients are discarded.

the mean-field remains at the same magnitude with the further increase of N. With a much slighter increase of a, the mean-field comes to oscillate more regularly, whereas the motion is scattered around torus motion (Fig. 3).

The choice of plotting only every second or seventh step in Fig. 3 is not arbitrary but there is a reason for it, which will be clarified in the following sections. Our goal in this paper is to give a consistent explanation for the above collective motion. We try to answer the remaining questions in the collective dynamics: When the system size N goes to infinity, i.e., in the thermodynamic limit, how is the macroscopic dynamics characterized? How does the remnant order in high-dimensional collective dynamics emerge out of the completely desynchronized elements? How is a longer-time scale in the collective dynamics formed? How does the collective dynamics depend on the parameters a and ϵ, and what kind of bifurcation structure is expected, and how is it explained in terms of dynamical systems theory?

4. Thermodynamic limit of collective motions

4.1. Amplitude of collective motion

In Section 3, we have mentioned that the mean-field dynamics plotted in the return maps shows some structures, ranging from lower-dimensional structures, such as a torus, to higher-dimensional stochastic structures. First of all, to characterize the mean-field dynamics, we compute the mean-square deviation (MSD) of the mean-field distribution,

$$\langle (\delta h)^2 \rangle = \langle h^2 \rangle - \langle h \rangle^2, \tag{4}$$

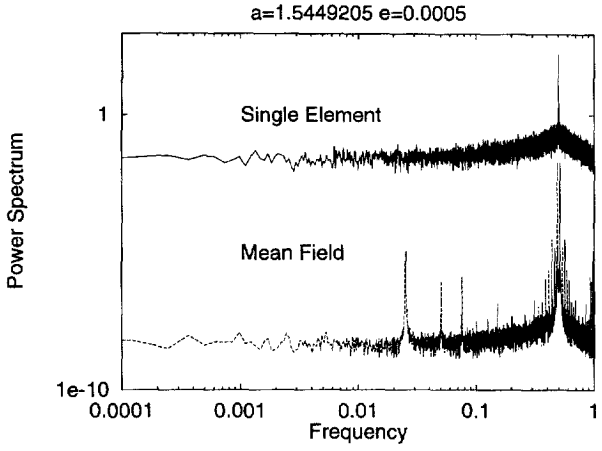

Fig. 2. Power spectrum of time series of a single element $x_n(i)$ (upper) and the mean-field h_n (lower), $a = 1.5449205$, $\epsilon = 0.0005$, $N = 10^7$. While the spectrum for a single element has a peak at the frequency 0.5, continuous component is much larger than that of the mean-field dynamics. Hence, the mean-field dynamics is more regular than the dynamics of each element. The slow dynamics of the mean-field is shown by the peak at the frequency 0.025269.

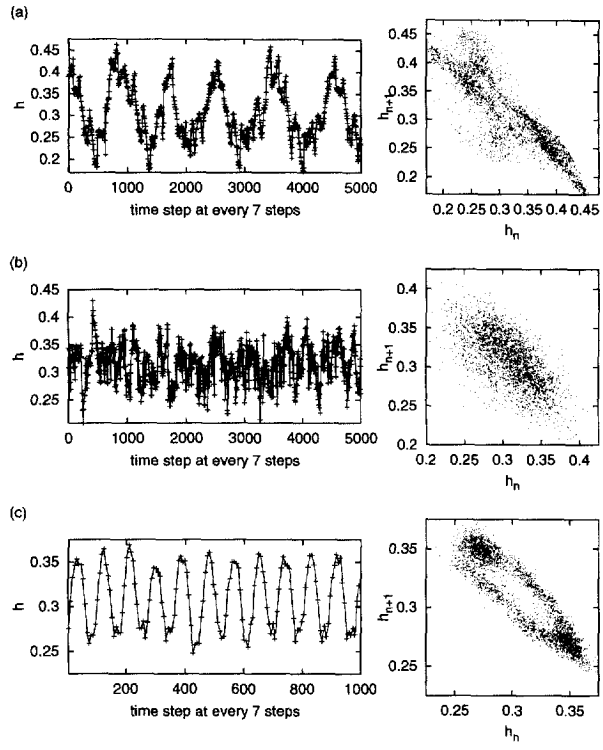

Fig. 3. Time series and return map. Time series are plotted at every seven steps. The parameters are $a = 1.69620$, $\epsilon = 0.008$, $N = 10^7$ (a), $a = 1.69755$, $\epsilon = 0.008$, $N = 10^7$ (b), $a = 1.69844$, $\epsilon = 0.008$, $N = 10^7$(c).

as a measure of the amplitude of the mean-field dynamics. The bracket $\langle\cdot\rangle$ denotes the temporal average.

When the mean-field does not have clear structure as in the case of Fig. 3(b), the MSD is useful to measure the variation around the fixed point. On the other hand, when the mean-field dynamics shows quasiperiodic motion as shown in Section 3, it would be reasonable to define the amplitude distinguished from "noisy component". As we will see in Section 4.2, however, such separation is impossible, because the "noisy component" does not get smaller with the increase of system size N. Even in this case, the MSD can roughly measure the size of the collective motion.

In Fig. 4 the MSD of the mean-field is plotted with the system size N, which converges to some limit for $N \to \infty$. These show the distinction of the mean-field dynamics from pure noise and suggest some coherence among elements.

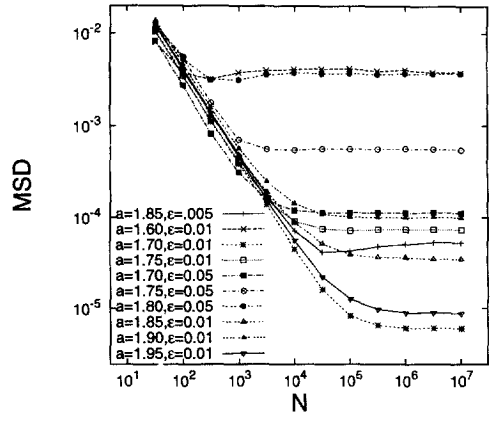

Fig. 4. Mean square deviation (MSD) of the mean-field distribution $\langle(\delta h)^2\rangle = \langle h^2\rangle - \langle h\rangle^2$ are plotted as a function of the system size N.

4.2. Degrees of freedom of collective motion

Next, we study the number of degrees of freedom in the collective dynamics in the thermodynamic

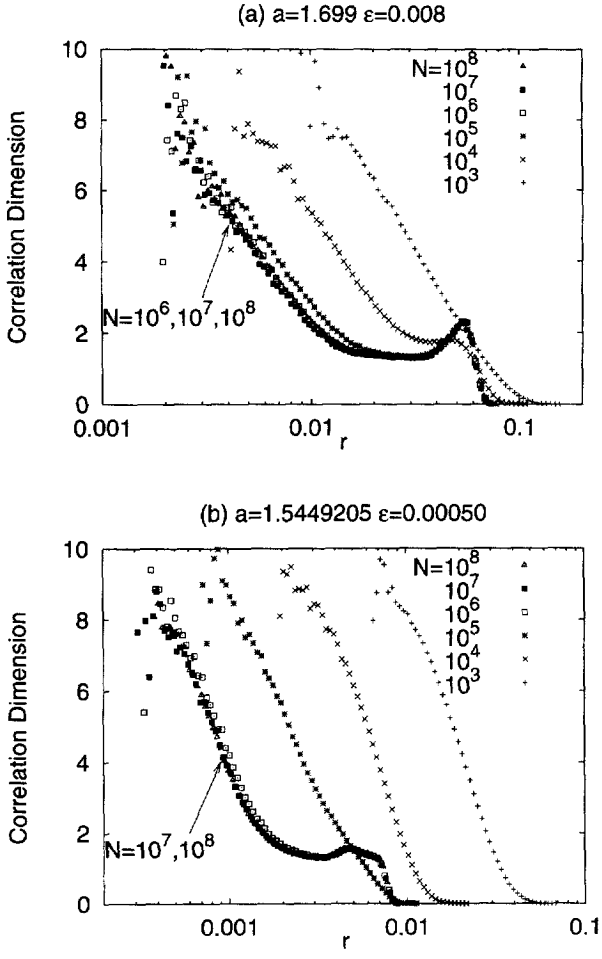

Fig. 5. Correlation dimensions are plotted as a function of scale size r for different system size, which are indicated at the right of each figure. The mean-field time series is embedded into 10-dimension. The parameters are $a = 1.699$, $\epsilon = 0.008$ (a), and $a = 1.5449205$, $\epsilon = 0.00050$ (b).

limit. In the previous section, we have mentioned that the collective motion, detected in the return map, has some low-dimensional-like structure but the width of scattered points around the 'torus' remains finite in the thermodynamic limit. Since the possibility of the present higher-dimensional torus is not excluded only by the figure, we have measured the correlation dimension [25] of the mean-field time series.

In Fig. 5, the change of slope in the correlation integral $(\mathrm{d}\log C(r))/(\mathrm{d}\log r)$ is plotted as a function of the scale size with increasing the system size N. For a smaller system size, the correlation dimension increases monotonically for decreasing the scale as for random variables. For a lager system size, curves have a plateau at a value less than the correlation dimension 2, which seems to correspond to collective motion. In a smaller scale, however, the correlation dimension becomes large. At this smaller scale, the motion is hard to be distinguishable from noise. If the scale of this regime would get smaller with the size N, one could conclude that the collective dynamics is low-dimensional in the thermodynamic limit. As shown in Fig. 5, this is not the case. The slope function converges to a certain curve with the increase of size N, where the plateau region does not get wider. Thus, the mean-field dynamics does not converge to lower dimensional dynamics in the thermodynamic limit.

To check the validity of this method, it may be relevant to mention the case of a heterogeneous system [18], e.g., a globally coupled map with a distributed nonlinearity parameter a over elements. In such a GCM the mean-field dynamics shows a clear quasiperiodic motion. The width of scattered points around the tours converges to 0 in the thermodynamic limit. Corresponding plots of slopes are given in Fig. 6, where the plateau at the value 1 is expanded with N, and the "noise" region is shrieked to the

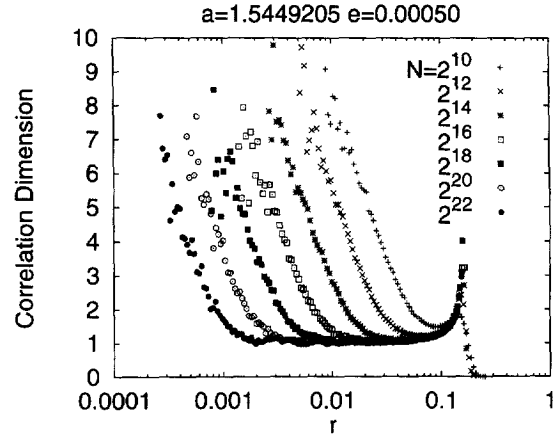

Fig. 6. Correlation dimension for heterogeneous GCM [18]. The parameters are $a = 1.9, \epsilon = 0.11$. Nonlinearity parameter for each element is homogeneously distributed over $a \in [1.875, 1.925]$. The mean-field time series is embedded into 10-dimension.

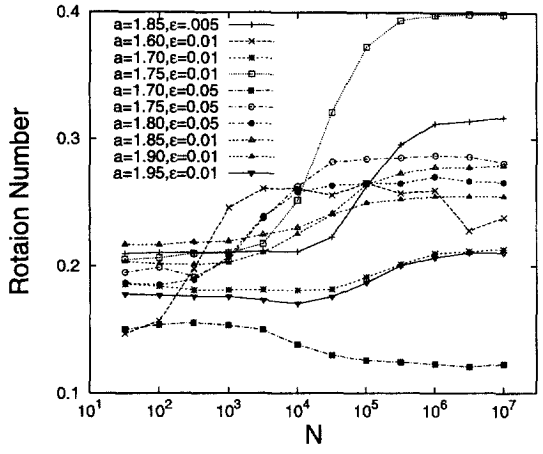

Fig. 7. Rotation number R of the mean-field dynamics, plotted as a function of system size N.

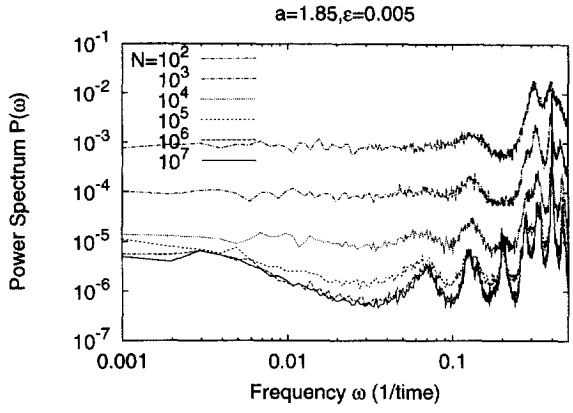

Fig. 8. Power spectrum for the mean-field dynamics with the increase of system size N. $a = 1.85$, $\epsilon = 0.005$.

scale $r \approx 0$. The difference from our uniform case is clearly visible. [3]

4.3. Characteristic timescale of collective motion

To see how the timescale of the mean-field dynamics depends on the system size N, we measure the rotation number of the mean-field dynamics as a function of the system size N. Here, the rotation number R is defined as

$$R = \lim_{t\to\infty} \frac{1}{t} \sum_{n=1}^{t} \frac{\Delta\theta_n}{2\pi}, \tag{5}$$

where $\Delta\theta_n$ is the angle variable formed by the two vectors $(h_n - \langle h\rangle, h_{n+1} - \langle h\rangle)$, and $(h_{n+1} - \langle h\rangle, h_{n+2} - \langle h\rangle)$ defined around the average mean-field $\langle h\rangle$ over time.

In most cases, the rotation number seems to converge to a certain value (Fig. 7). It is suggested that the mean-field dynamics approaches certain dynamics, independently of the system size for large enough N. In Fig. 8, the power spectrum of the mean-field dynamics has some peaks. The low frequency component around 0.07 corresponds to the collective dynamics, while the high frequency component around 0.4 represents the element dynamics, as will be clear in Section 5.

This section is summarized as follows. In Fig. 5, the correlation dimension shows a plateau within the middle scale. This plateau corresponds to the lower-dimensional dynamics, that is shown in the return maps (Figs. 1 and 3). For larger values of N, the MSD and the rotation number are characterizations of this collective motion.

5. Global phase diagram of collective motion in parameter space: tongue-like bifurcation structures

In this section, we will study the dependence of the amplitude of the collective motion of the parameters a and ϵ.

In Fig. 9, the MSDs are plotted as a function of the parameter a for several coupling strengths ϵ. Here the system size is chosen to be large enough, to see the behavior of the MSD converged in the thermodynamic limit. Two points should be noted here. First, the change of the MSD is not monotonic with a, but is rather complicated. Second, the change of the MSD is complicated with fine structures, which still keep some similarity against the changes of the coupling strength ϵ. For example, a similar but slightly different structure is visible for $a \approx 1.7025$ for $\epsilon = 0.01$, $a \approx 1.715$ for $\epsilon = 0.015$, and $a \approx 1.73$ for $\epsilon = 0.02$.

[3] In the heterogeneous case, the law of large numbers is recovered around the torus motion.

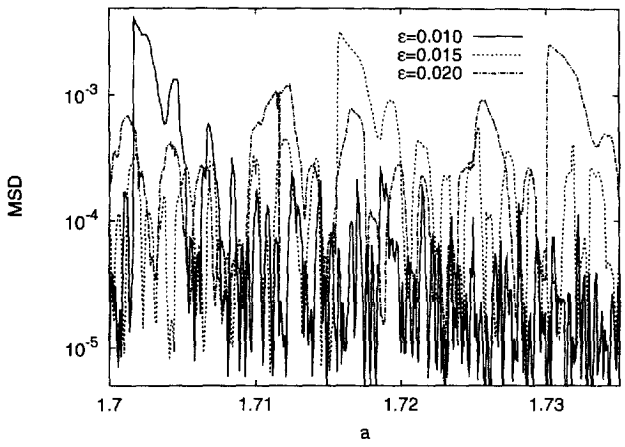

Fig. 9. Mean square deviation (MSD) of the mean-field dynamics is plotted as a function of a. $\epsilon = 0.02, 0.15$ and 0.01. $N = 2^{16}$.

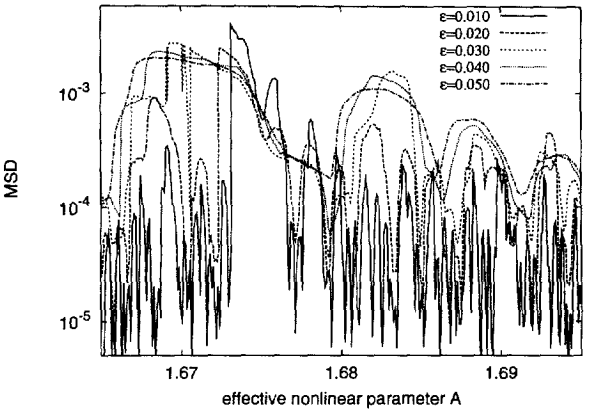

Fig. 10. Mean square deviation (MSD) of the mean-field dynamics h_n plotted as functions of the effective nonlinearity parameter A.

To see the structure in the parameter space closely, we introduce rescaling of the parameters. For it, we note that each element obeys the following dynamics:

$$x_{n+1} = (1-\epsilon)(1-ax_n^2) + \epsilon h_n, \tag{6}$$

where h_n is the mean-field value at time step n, which can modify the nonlinearity of each element effectively.

Usually, the deviation of the mean-field around the mean-field average $\langle h\rangle = \lim_{t\to\infty}(1/t)\sum_{n=0}^{t} h_n$ is small. Hence it seems reasonable to normalize the variable x_n so as to separate $\langle h\rangle$ from h_n. Introducing scaled variable $X_n = x_n/(1-\epsilon+\epsilon\langle h\rangle)$, the dynamics of each element is given by

$$X_{n+1} = 1 - AX_n^2 + \kappa\delta h_n, \tag{7}$$

where $\delta h_n = h_n - \langle h\rangle$, and A and κ are called "effective nonlinear parameter" and "effective coupling strength", respectively, given by

$$A = (1-\epsilon)(1-\epsilon+\epsilon\langle h\rangle)a, \tag{8}$$

$$\kappa = \frac{\epsilon}{1-\epsilon+\epsilon\langle h\rangle}. \tag{9}$$

In Fig. 10 we have plotted the MSD by adopting the effective nonlinearity parameter A instead of a. Note that similar structures with a different value of a in Fig. 9 are overlapped around a certain value of A in Fig. 10. For smaller ϵ, finer structures can be seen in a broader structure for larger ϵ. In Fig. 11(a) the parameter dependence of the MSD is plotted on the two-dimensional (A, κ)-plane. Regimes with the collective motion with a larger amplitude (i.e. larger variance) form tongue-like structures[4] (called "tongue structure"), each of which starts at some point or interval of parameter A at $\kappa = 0$, and grows with κ. The scaling structure of tongues seems to be clearer. While the width of each tongue seems to increase roughly linearly with A and κ, detailed discussion will be given in Section 8.

When the effective coupling strength κ approaches 0, each tongue structure corresponds to a window of the single logistic map (Fig. 11(b)). For instance, between $A \approx 1.75$ and $A \approx 1.79$ a tongue structure can be clearly seen in Fig. 11(a), corresponding to the period-3 window of the single logistic map. Although there is a countably infinite number of windows in the parameter space of the logistic map, it is difficult to detect the windows for a longer period numerically. However, it is remarkable that a lot of tongue structures are visible in our model, corresponding to the windows with a longer period.

In each tongue structure, further internal structures exist. For instance, the tongue corresponding to period-3 window of the logistic map between

[4] Similar structures are also observed in a globally coupled tent map [20].

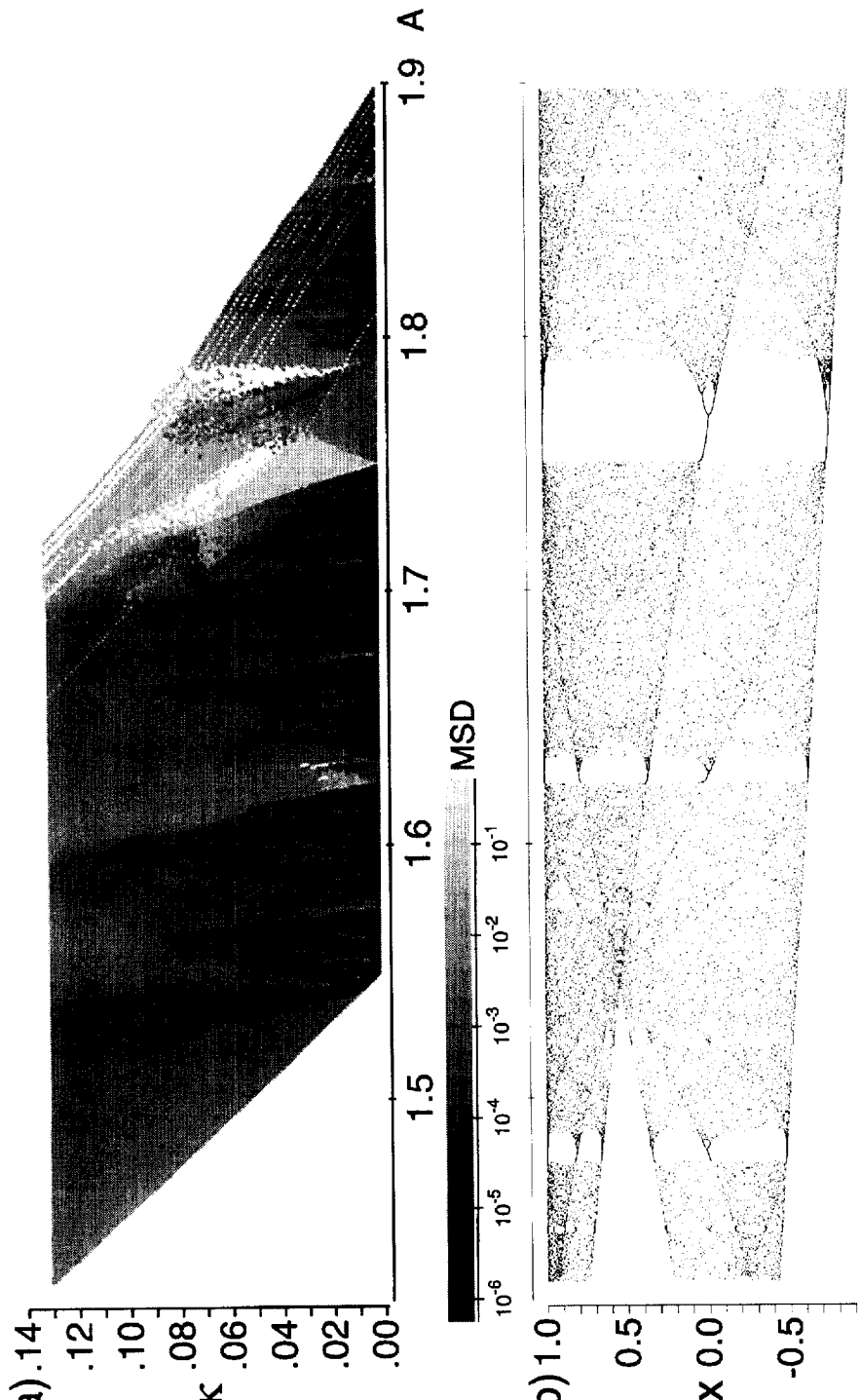

Fig. 11. (a) The Mean square deviation (MSD) of the mean-field dynamics plotted as a function of the effective nonlinearity parameter A and κ. The scale shows the value of the MSD, where the darkest one corresponds to MSD $\approx 10^{-6}$, and the brightest one to MSD $\approx 10^{-1}$. (b) Logistic map bifurcation diagram with the increase of the nonlinearity parameter. Horizontal axes are common among the two figures.

$A \approx 1.75$ and $A \approx 1.79$, has three internal structures, roughly speaking. To understand the inner structure in each tongue, in the following two sections we will study the dynamics of each element and its distribution.

6. Collective behavior through self-consistent dynamics

In this section, we will briefly describe how the collective motion is formed, focusing on the tongue structure.

6.1. Distribution dynamics

In the limit of $N \to \infty$, the probability distribution function is defined as follows:

$$\rho_n(x) = \lim_{N\to\infty} \frac{1}{N} \sum_i \delta(x - x_n(i)). \tag{10}$$

The mean-field dynamics oscillates, instead of converging to a fixed point. This implies that the probability distribution function does also not remain stationary but depends on time.

In Fig. 12, the evolution of the probability distribution function is shown, using numerical calculation.

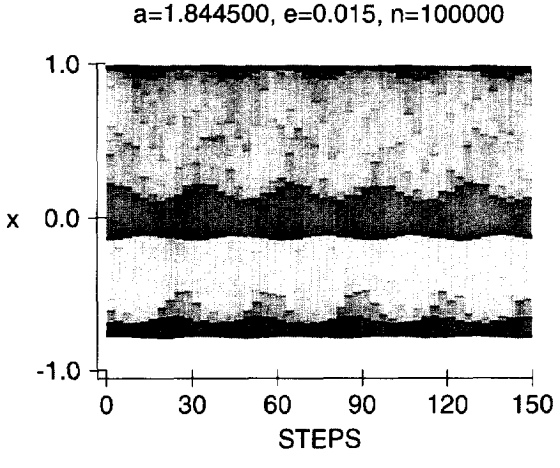

Fig. 12. The distribution dynamics plotted as a function of time. The density is shown with the use of a gray scale. The darker region indicates the higher density. The parameters are $a = 1.8445$, $\epsilon = 0.015$, $N = 10^5$.

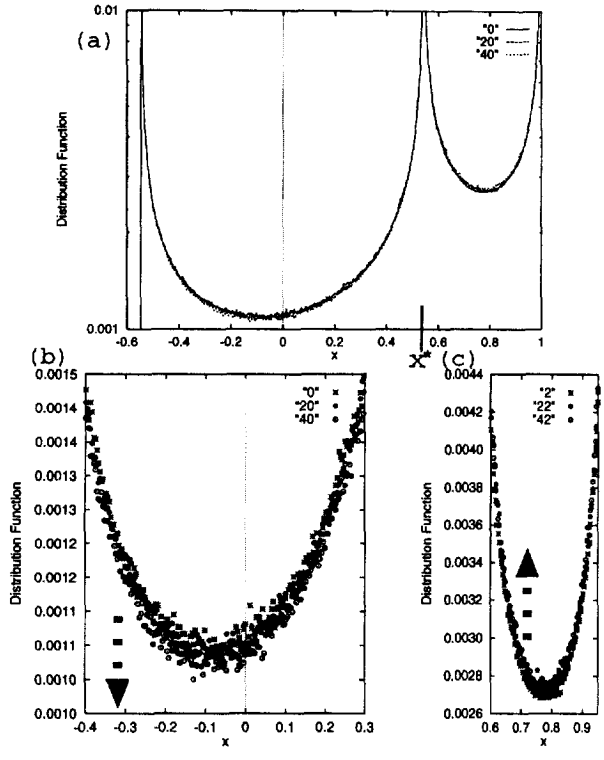

Fig. 13. The distribution functions at time $n = 0$ (∗), 20 (•), 40 (○).

The parameters for the figure ($a = 1.8445$, $\epsilon = 0.015$) belong to the tongue structure in the period-3 window. Since the mean-field dynamics has a component of period-3, in the figure the density is plotted every third step in order to see the slow modulation of $\rho_n(x)$. Due to the chaotic oscillation of each element, the distribution function spreads over $x \in [-0.8, 1.0]$, but the distribution is not monotonous, and has some structure. In the three regions around $x \approx 1.0$, $x \approx 0.0$ and $x \approx -0.8$, the density is relatively large. This number "3" is the period of the window in the logistic map for the corresponding tongue structure. The number of elements in each of the three regions oscillates in time, and the phase of each oscillation is mutually different.

6.2. Formation of self-consistent dynamics

It is interesting to study the collective dynamics as an interference between mean-field dynamics and

individual elements. Before we present a scenario for collective motion, we show the formation of self-consistent dynamics between the mean-field dynamics and individual elements.

For simplicity, we adopt the case, in which the effective nonlinearity parameter A is near the period-2 band merging point. The time series and the return map are given in Fig. 1. The distribution function is given in Fig. 13 every 20th step. In this case, distribution of elements can be divided into two regions around $x^* \approx 0.54$. During these 40 time steps the density at the left region ($x < x^*$), given in Fig. 13(b), decreases with time, whereas the density in the other region plotted in Fig. 13(c) increases with time. Although the change of the distribution is quite small, there is a systematic oscillation (cf. Fig. 18).

Consider the density dynamics in each of the two regions. In Fig. 14(a), the density in each region, N_L and N_R are plotted as a function of time. N_L denotes the probability in the region smaller than x^* in Fig. 13, and $N_R(= 1 - N_L)$, i.e. $N_L = \int_{x<x^*} \rho_n(x)\,dx$, and $N_R = \int_{x>x^*} \rho_n(x)\,dx = 1 - N_L$. (The definition for each region is given below in detail.) The distribution in each region oscillates in time. In Fig. 14(b), the mean-field time series h_{n-1} and h_n are plotted at every two steps, since the mean-field has a period-2 component. The mean-field also oscillates in time

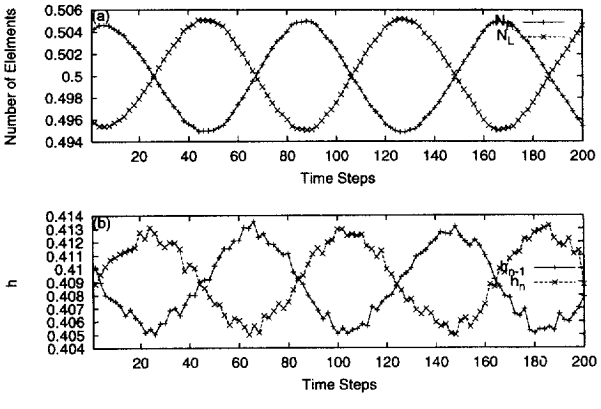

Fig. 14. (a) Time series of the number of elements in the two regions. (b) Time series of the mean-field. $a = 1.5449205$, $\epsilon = 0.0005$, $N = 10^6$.

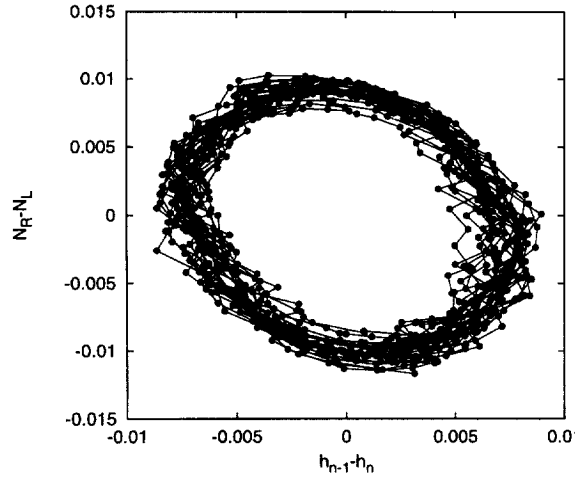

Fig. 15. Return map of the time series of the number of elements in the two regions and time series of the mean-field, plotted per two steps for even n and odd n. $a = 1.5449205$, $\epsilon = 0.0005$, $N = 10^6$.

with the same period as N_R, and N_L, but the phase of the mean-field oscillation is different from that of the population dynamics in Fig. 14(a).

To see how the mean-field dynamics and the distribution dynamics interfere with each other, we have constructed a return map of the above two quantities. Fig. 15 gives a return map of the distribution dynamics and the mean-field dynamics. This figure implies that a self-consistent dynamics is formed as follows:

$$\begin{aligned} \tilde{h}_n &= \tilde{h}(\tilde{h}_{n-1}, \tilde{N}_{n-1}), \\ \tilde{N}_n &= \tilde{N}(\tilde{h}_{n-1}, \tilde{N}_{n-1}), \end{aligned} \tag{11}$$

where each $\tilde{h}$ and $\tilde{N}$ is a function of $\tilde{h}_n = h_{n-1} - h_n$ and $\tilde{N}_n = N_L - N_R$. If the mean-field would be an external force for each element, the population would respond to the mean-field value. Since the distribution organizes the mean-field dynamics, the collective motion can be described as a self-consistent relation between the distribution dynamics and the mean-field dynamics.

From the above viewpoint, we demonstrate now how the distribution is modified as the mean-field varies slowly.

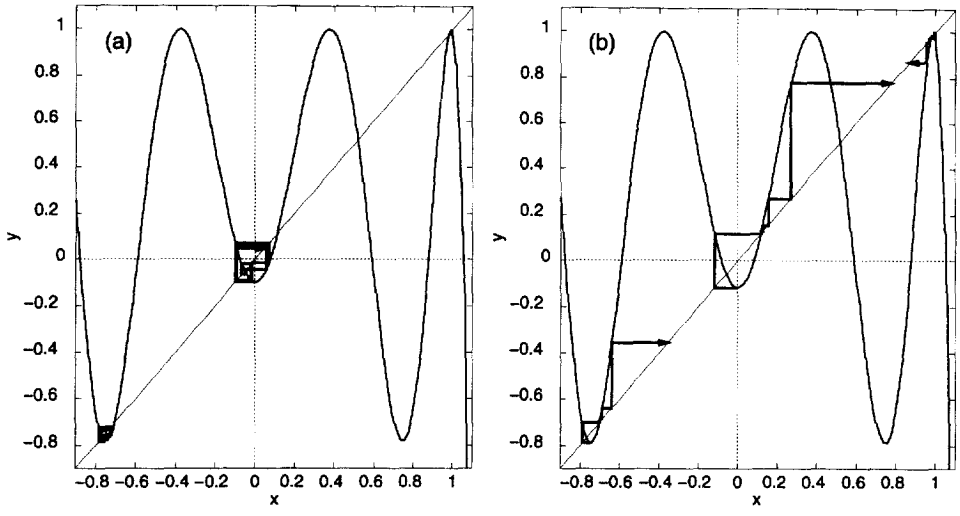

Fig. 16. Behavior of the third iterate of a logistic map: (a) after tangent bifurcation at three points, and (b) after crisis. Solid lines with arrow indicate iterated trajectories starting from three points.

6.3. *Internal bifurcation in temporal domain*

If the mean-field would be an external force for each element, we could study the dynamics of each element as the logistic map with an external force. This is valid if the mean-field varies slowly. In this case, the equation of motion for each element is given by

$$x_{n+1} = F_n(x_n), \tag{12}$$

with

$$F_n(x) = (1-\epsilon)(1-ax^2) + \epsilon\langle h\rangle + \epsilon\delta h_n. \tag{13}$$

If we would not take δh_n into account, the dynamics of each element would be the same as the dynamics of the logistic map. Since each tongue structure has good correspondence with a window of the logistic map as shown in Section 5, we focus on the window structure of the logistic map. In the single logistic map, the period-p window starts at the tangent bifurcation point of the pth iterate of the map, and then the period doubling bifurcation proceeds with the increase of a, until the window ends up by crisis (see Fig. 16). In this case, the probability distribution is stationary, and hence, the probability that an element takes a value out of p distinct regions is $1/p$.

Now, take δh_n in Eq. (13) into account as an external force. The bifurcation of the perturbed logistic map (13) has a crucial difference from usual bifurcation of the logistic map. In Fig. 17, examples of the third iterates of the map with external force are shown. In Fig. 17(a) the region around $x \approx 0$ can attract the elements, while the two regions around $x \approx 0.95$ and $x \approx -0.75$ cannot. In Figs. 17(b) and (c), while three regions cross the line $y = x$, one or two of the regions collapses due to crisis. At the tangent bifurcation, the map $y = F_n^{(3)}(x)$ is tangential to $y = x$ at only one point. This is in strong contrast with the logistic map without external force, where tangent bifurcation or crisis occurs at three-points of x at the same value of a and ϵ for the period-3 window.

In general, consider a period-p window. In the presence of the external force, for each of the p points in the pth iterate of the map (13), the tangent bifurcation, or crisis occurs at different value of a and ϵ. Hence, the number of distinct attractors can be less than p, and depending on a and ϵ. Even if the elements are attracted into p distinct regions, the probability for each of p distinct regions is not equal to $1/p$.

As we have seen in Section 6.2, slow modulation of the mean-field leads to the dynamics of

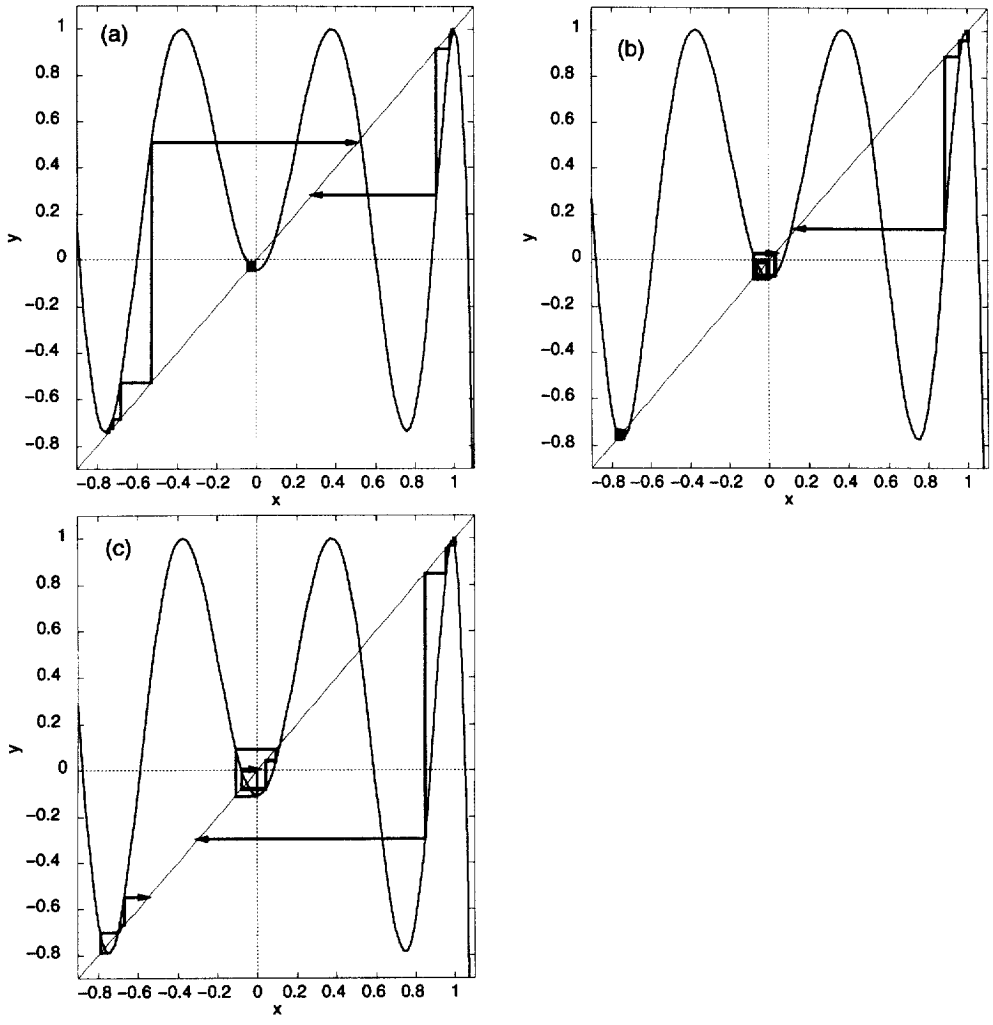

Fig. 17. Behavior of the third iterate of a logistic map with period-3 external force. In contrast with the case of Fig. 16, only one or two regions can attract trajectories. (a) The region around $x = 0$ attracts orbits as a region after tangent bifurcation, while the other regions, which are before the tangent bifurcation, cannot attract orbits. (b) Two regions around $x = 0$, and $x = -0.8$ attract orbits, while the region around $x = 1.0$ cannot attract orbits due to the crisis. (c) The region around $x = 0$ attracts orbits, while the other regions cannot attract orbits due to the the crisis.

the distribution. With the slow modulation of δh_n in time, the behavior of each element changes as well. In other words, with the change of δh_n, bifurcation can occur in the effective map for each element,

$$F_n^{(p)} = F_n \circ F_{n-1} \circ \cdots \circ F_{n-p+1}, \tag{14}$$

which is the pth iterate of the map (Eq. (13)). Since δh_n changes over time, such a bifurcation occurs in time. To distinguish this bifurcation from the notion of bifurcation in parameter space, this type of bifurcation is called "internal bifurcation".[5]

[5] In our previous work [18], the nonlinearity parameter a was distributed over elements. In that case, some sort of differentiation of dynamics over elements enabled the collective motion. To characterize the differentiation, the notion of "internal bifurcation" was introduced as a snapshot representation of one

To characterize the effective map at every p time steps, we introduce the invariant measure $P_n^{(p)}(x)$ at time n determined by the solution of the Perron–Frobenius equation,

$$P_n^{(p)}(x) = \int_{-1}^{1} P_n^{(p)}(y)\delta(x - F_n^{(p)}(y))\,dy. \tag{15}$$

If $P_n^{(p)}(x)$ changes slowly, the difference $\rho_n(x) - P_n^{(p)}(x)$ decreases with time.

On the other hand, a change in $\rho_n(x)$ can lead the mean-field $h_n = \int f(x)\rho_n(x)\,dx$ to a certain critical value, at which the internal bifurcation occurs in the effective map, Eq. (14). For instance, a small difference of the mean-field induces the effective map to be tangential to the line $y = x$ at one point, or it induces one region of the effective map to be collapsed by crisis. As a result, the nature of the invariant measure $P_n^{(p)}(x)$ of the effective map changes qualitatively. This drastic change in $P_n^{(p)}(x)$ occurs, before $\rho_n(x)$ approaches $P_n^{(p)}(x)$. So, $\rho_n(x)$ cannot be close to $P_n^{(p)}(x)$.

With this internal bifurcation, the distribution $\rho_n(x)$ does not actually approach $P_n^{(p)}(x)$, because (1) the velocity of change $\rho_n(x)$ is finite, and (2) the change of $\rho_n(x)$ results in the qualitative change of $P_n^{(p)}(x)$. Consequently $\rho_n(x)$ oscillates in time. This qualitatively explains why the mean-field does not approach a fixed point[6] at the thermodynamic limit.

Let us look again at the example in Section 6.2 and try to describe the dynamics under the above scenario. Since the effective nonlinearity parameter A is near the band merging point of the single logistic map, it is useful to define the two regions shown in Fig. 14, that correspond to the two bands of the logistic map near the band merging point. The effective dynamics is given by the second iterate of map,

$$F_n^{(2)}(x) = (1-\epsilon)(1 - a\{(1-\epsilon)(1-ax^2) + \epsilon h_{n-1}\}^2) + \epsilon h_n. \tag{16}$$

system. As we will show below, we extend the notion of "internal bifurcation" to the present identical case.

[6] The unstable fixed point of the mean-field value is given as $h = \int f(x)\rho_0(x)\,dx$, where $\rho_0(x)$ is a fixed point solution of Eq. (15) with $p = 1$. The fixed point solution $\rho_0(x)$ is unstable.

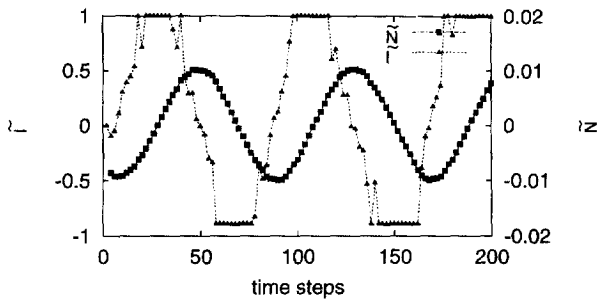

Fig. 18. Temporal change of $\tilde{N}_n = N_L - N_R$ and $\tilde{I}_n = I_L - I_R$, where $N_L = \int_{x\in L} \rho_n(x)\,dx$, $N_R = 1 - N_L$, $I_L = \int_{x\in L} P_n^{(2)}(x)\,dx$ and $I_R = 1 - I_L$, are plotted as a function of time step. See text for the region L and R. $a = 1.5449205$, $\epsilon = 0.0005$, $N = 10^6$.

The lines $y = F_n^{(2)}(x)$ and $y = x$ cross at three points within $x \in [-1, 1]$ when $a < 2$ and $\epsilon > 0$. The middle of these points is denoted by x_n^*. R and L denote the regions where $x > x_n^*$ and $x < x_n^*$, respectively.[7]

Consider the case where A is near the band merging point of the single logistic map. If the mean-field would be on an unstable fixed point, these two regions would collapse due to crisis. As we have discussed above, however, the dynamics of the mean-field modulates the effective map, Eq. (16). As a result, for this parameter regime, there are two cases: (1) the modulation of the map is large enough, so that the R region is an "unstable region", while the L region is a "stable region" (and vice versa), and (2) the modulation of the map is small, so that both the L and the R regions are "unstable regions". Here, we use the term "stable" and "unstable" as follows. Consider a trajectory starting from a region obtained by the iteration of the map $y = F_n^{(2)}(x)$ at a certain time step n. If the trajectory stays within the region, we call the region "stable region". If the trajectory leaves the region, we call the region "unstable region". By analyzing the map $y = F_n^{(2)}(x)$, we can always determine the "stability of regions" at each time step.

In Fig. 18, the oscillation of population in these two regions is shown as $\tilde{N}_n = N_L - N_R$ (see also Figs. 14

[7] Note that if we would not take δh_n into account, i.e. $h_n = \langle h \rangle$, x^* would be independent of time and x^* would denote the period-1 unstable fixed point of the single logistic map.

and 15). In Fig. 18, the deviation of invariant measure $P_n^{(2)}(x)$ in the two regions, i.e. $\tilde{I}_n = I_L - I_R$, where $I_L = \int_{x\in L} P_n^{(2)}(x)\,dx$ and $I_R = 1 - I_L$, is also plotted as a characterization of effective map (16). During the time steps $n \in [6, 46]$, $\rho_n(x)$ approaches $P_n^{(2)}(x)$, until the change of $\rho_n(x)$ induces $P_n^{(2)}(x)$ to change qualitatively at time step $n = 46$. This qualitative change in $P_n^{(2)}(x)$, and consequently the qualitative change in the effective map is due to crisis in the L region. In this way, the stability of the regions changes and some elements in the L region move to the R region. As a result, the distribution $\rho_n(x)$ approaches $P_n^{(2)}(x)$ again, until the next crisis enables a flow from the R region to the L region.

To sum up, the distribution function $\rho_n(x)$ changes slowly, in this way approaching $P_n(x)$ until the modulation of the mean-field changes the internal bifurcation structure qualitatively. In this example, the qualitative change in the internal bifurcation structure is due to local crisis. As a result of the change of the internal bifurcation structure in the two regions, the elements are attracted to a different region. With the repetition of this stability change of the regions, the mean-field oscillates quasiperiodically. This mechanism of change in each band holds for any period-p band (window) regime, where elements are attracted to and repelled from each band region successively with the internal bifurcation.

7. Bifurcation of collective motion

7.1. Bifurcation of tongue structures

As we have seen in Fig. 18 in Section 6.3, one of the two regions in the second iterate of the effective map, Eq. (16), collapses due to crisis and the stability of the regions changes in time. In this Section, we will show that with the increase of A, the time interval during which the regions are unstable becomes longer.

There are three kinds of time intervals. In one case, both of the two regions R and L, defined in Section 6.3, are stable. $P_n^{(2)}(x)$ is positive for the two regions but there is no connection between the two positive regions. In the second case, only one of the two regions

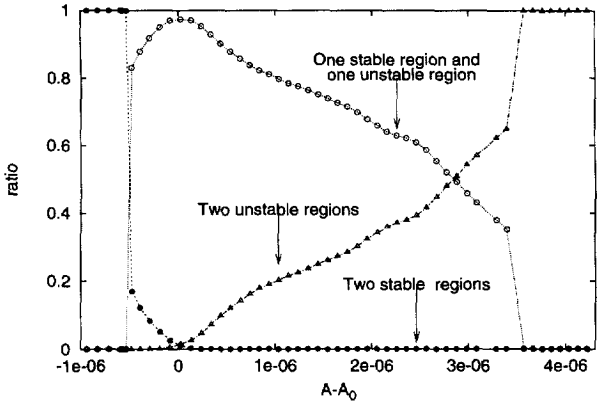

Fig. 19. Ratio of the time steps, in which both the two regions collapse (△), one of the two regions collapses (○), and none of the two regions collapses (•). $A_0 = 1.5436890$ (band merging point), $\epsilon = 0.0005$, $N = 10^7$. The collapse is due to the crisis bifurcation in internal bifurcation.

is unstable, and $P_n^{(2)}(x)$ is positive for one region and zero for the other. In the third case, both of the two regions are unstable. $P_n^{(2)}(x)$ is positive for the two regions and there is continuous connection between them. The ratios of these time intervals are plotted in Fig. 19 as a function of $A - A_0$, where A_0 is the parameter for the band merging point of the logistic map. For $A - A_0 \leq -0.6 \times 10^{-6}$ crisis never occurs in both the two regions L and R, whereas for $A - A_0 > -0.6 \times 10^{-6}$, the time interval during which the regions are unstable gets longer. For the parameter beyond $A - A_0 = 3.6 \times 10^{-6}$, the two regions are unstable due to crisis bifurcation for every time step. Hence, the period-2 tongue structure starts at the parameter $A - A_0 \cong -0.6 \times 10^{-6}$, where one of the two regions of the effective map, Eq. (16), becomes unstable for some time steps. It ends at the parameter $A - A_0 \cong 3.6 \times 10^{-6}$, where both the two regions become unstable all the time due to the crisis.

Consider an internal bifurcation condition of Eq. (14) (for instance, crisis or tangent bifurcation in each element.). For $\epsilon = 0$ the bifurcation condition holds at a single parameter value. For $\epsilon > 0$, due to the oscillation of the mean-field, within the parameter interval $A_{\text{small}}(\epsilon) < A(\epsilon) < A_{\text{large}}(\epsilon)$ in the (A, ϵ)-parameter space, the internal bifurcation condition is

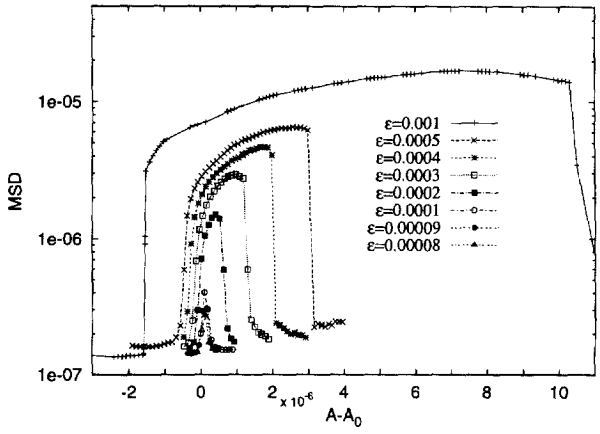

Fig. 20. Mean square deviation (MSD) of the mean-field distribution with the increase of ϵ plotted as a function of the effective nonlinearity parameter A. The region corresponds to the period-2 tongue structure. A_0 denotes the band merging point (crisis bifurcation point of 2-band) of the logistic map ($A_0 = 1.5436890126$).

satisfied for some steps. Hence, the edge of a tongue structure starts at $\epsilon = 0$ from tangent bifurcation point and crisis bifurcation point. It is extended into the parameter space for $\epsilon > 0$, where each bifurcation condition is satisfied during some time steps (see Fig. 20 for period-2 tongue structure). The scaling of the width of the tongue structure will be discussed in Section 8.

7.2. *Bifurcation in a tongue structure*

Even within one tongue structure, we can observe different types of collective motion. With the change of the parameter A and κ, in the collective dynamics a kind of bifurcation occurs. Since the collective dynamics remains high-dimensional, it is not described as a standard bifurcation in low-dimensional dynamical systems. Here we study a mechanism of such a change in the collective dynamics.

In Section 3, it is shown that a slight increase in a induces a qualitative change of the collective dynamics (Fig. 3). To see this quantitatively, it may be convenient to measure the rotation number of the collective dynamics. In Fig. 21, the rotation number is plotted as a function of A. In the regime plotted in the figure, a period-7 tongue structure is observed between $A - A_0 \in [-0.744 \times 10^{-3}, 1.499 \times 10^{-3}]$, where A_0

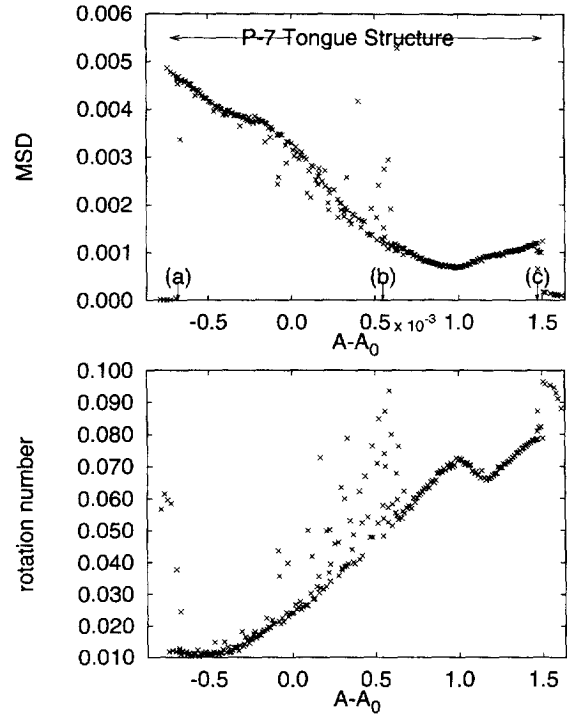

Fig. 21. Mean square deviation (MSD) and rotation number of the mean-field dynamics are plotted as a function of $A - A_0$, where $A_0 = 1.67407$ denotes the tangent bifurcation point of period-7 window. In the figure (a), the parameters $a = 1.6962$, 1.69755, and 1.69844 are indicated as (a), (b) and (c), corresponding to the parameters in Figs. 3 and 22.

denotes the tangent bifurcation point of the period-7 window of the logistic map. Typical examples of the collective dynamics are shown in Fig. 3.

As we have already introduced in Section 6.3, the invariant measure $P_n^{(7)}(x)$ of the effective map,

$$F_n^{(7)} = F_n \circ F_{n-1} \circ \cdots \circ F_{n-6}, \tag{17}$$

may be useful to see the change of the dynamics with the increase of A. In Fig. 22, three examples of $P_n^{(7)}(x)$ are plotted as a function of time.

For the parameter of Fig. 22(a), the parameter A is close to, but smaller than, the tangent bifurcation point of the period-7 window A_0. Therefore, if the fluctuations of the mean-field would be ignored, none of the seven regions could attract the elements because the seventh iterate of the logistic map, Eq. (17) would not cross the line $y = x$. With the influence of the

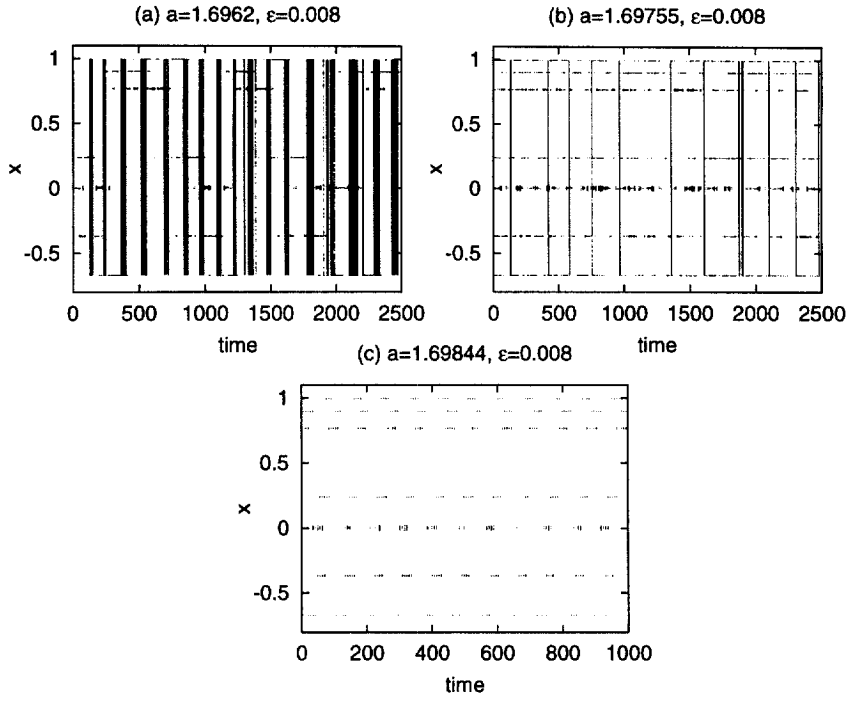

Fig. 22. Invariant measure of the effective map, Eq. (17), $P_n^{(7)}(x)$ plotted as a function of time. The horizontal axis is time and the vertical axis is x. In this figure, the region with $P_n^{(7)}(x) > 0$ is plotted by a solid line. When the whole region is filled by a line, none of the seven regions of the map, Eq. (17), cross the line $y = x$, and all the regions are connected as a single attracting set. In (a) and (b) some of the seven regions of the map, Eq. (17), cross the line $y = x$, while the other regions do not. In (c), on the other hand, all seven regions of the map, Eq. (17), cross the line $y = x$, while some of the seven regions are destabilized by crisis. The parameters correspond to those of Fig. 3.

mean-field dynamics, on the other hand, the effective map, Eq. (17), is modified to cross the line $y = x$ at a few regions where $P_n^{(7)}(x) > 0$ (for instance between $n = 2000$ and 2100 in Fig. 22(a)). These two or three regions can attract the elements until these regions come to be destabilized by crisis (for instance at $n \approx 2100$). After the crisis $P_n^{(7)}(x)$ spreads over the whole region because none of the seven regions of the map, Eq. (17), cross the line $y = x$. Then the regions attracting the elements switch to different positions. This process continues successively.

With the increase of A, the number of regions attracting the elements due to the tangent bifurcation of the map, Eq. (17), increases (Fig. 22(b)). In Fig. 22(b), 5, 6, or 7 regions are stabilized successively.

With the further increase of A, all the seven regions of the map, Eq. (17), always cross the line $y = x$, while some of these seven regions are destabilized by crisis (Fig. 22(c)). With the increase of A, for each of the seven regions, the time interval during which the region is unstable increases. The tongue structure ends at the parameter $A - A_0 = 1.499 \times 10^{-3}$, where all the seven regions are destabilized by crisis during every time step. Thus, the collective dynamics of the period-7 tongue structure ends. As a result, the amplitude of the mean-field dynamics reduces to about 0.1 (see Fig. 21).

Although we have explained the bifurcation in the internal tongue structure for the period-7 case, this kind of bifurcation structure is common to a band region in any period. For instance, in Fig. 11(a) with the period-3 tongue structure (starting from $A \in [1.75, 1.79032]$ at $\epsilon = 0$) and in the period-5 tongue structure (starting from $A \in [1.6244, 1.6333]$

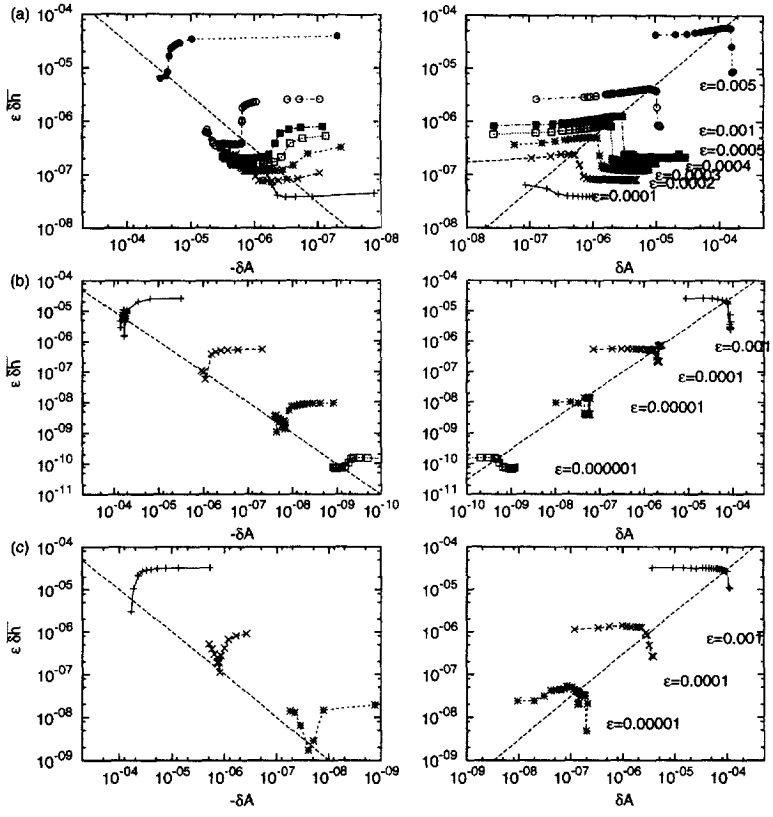

Fig. 23. Scaling relation of tongue structure for period-2 (a), period-3 (b), and period-5 (c). $\epsilon\delta h$ are plotted as functions of δA, where $\overline{\delta h} = \sqrt{\mathrm{MSD}}$ and δA indicate the deviation from the band merging point ($A = 1.5436890126$) (Fig. (a)), the crisis bifurcation point of period-3 window ($A = 1.7903274919$) (Fig. (b)), and the crisis bifurcation point of period-5 window ($A = 1.6333587036$) (Fig. (c)) of the logistic map, respectively. Line in each figure is proportional to δA. Hence, the edge of A in a tongue structure varies linearly with $\epsilon\delta h$. The width of a tongue structure increases proportional to $\epsilon\delta h$.

at $\epsilon = 0$), similar bifurcation structure is observed, where the change in the number of coexisting stable regions corresponds to such bifurcation structure.

8. Scaling of tongue structures

In this section, we study the growth of the width of a tongue structure with the increase of ϵ. Asymptotic behavior of the amplitude and the timescale of the mean-field structure with $\epsilon \to 0$ are also presented.

In a period-p tongue structure, the effective map for each element should be considered as

$$F_n^{(p)} = F_n \circ F_{n-1} \circ \cdots \circ F_{n-p+1} \tag{18}$$

with $F_n(x) = 1 - Ax^2 + \kappa\delta h_n$. Due to the fluctuation of δh_n, the nonlinear parameter in Eq. (18) effectively fluctuates within $[A - A_1\kappa\overline{\delta h}, A + A_1\kappa\overline{\delta h}]$ up to the first order of $\kappa\overline{\delta h}$. $\overline{\delta h} = \sqrt{\mathrm{MSD}}$ denotes the amplitude of the mean-field for a given set of parameters and A_1 is a certain positive constant determined by Eq. (18). In each tongue structure within $A(\kappa) < \varepsilon[A_{\mathrm{small}}(\kappa), A_{\mathrm{large}}(\kappa)]$, the same internal bifurcation, e.g. crisis or tangent bifurcation, occurs for some time steps. Therefore the inequality

$$A - A_1\kappa\overline{\delta h} < A_0 < A + A_1\kappa\overline{\delta h}, \tag{19}$$

is valid in the tongue structure, where A_0 denotes the bifurcation point of the single logistic map. Thus, A_{small} is the maximum parameter at which the second

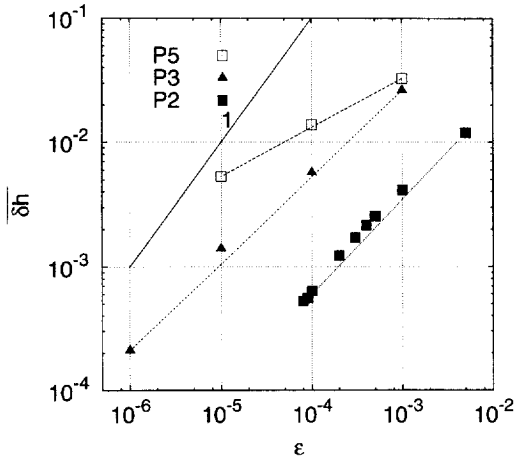

Fig. 24. Scaling relation of MSD with κ in the tongue structures. From the data shown in Fig. 23, the maximum values of $\overline{\delta h} = \sqrt{\text{MSD}}$ are plotted. They are obtained by sampling the data of the MSD by changing A in each tongue for a given ϵ.

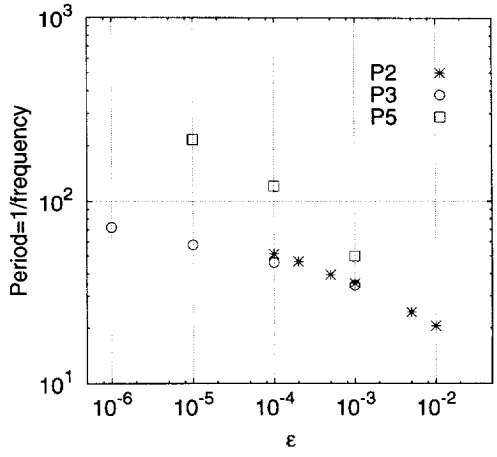

Fig. 25. The longer timescales of the mean-field dynamics plotted as a function of ϵ. They are obtained from the power spectrum for the parameter with maximum MSD value in the period-2, 3 and 5 tongue structure for a given ϵ.

inequality of Eq. (19) is violated, and A_{large} is the minimum parameter at which the first inequality of Eq. (19) does not hold. Hence, a single bifurcation point at $\kappa = 0$ splits into two lines, as is shown in Fig. 20, and the lines constitute a region,

$$A_0 - A_1 \kappa \overline{\delta h}_{A_{\text{small}}} < A < A_0 + A_1 \kappa \overline{\delta h}_{A_{\text{large}}}. \qquad (20)$$

In Fig. 23, tongue structures around the parameter A at the crisis bifurcation point of the period-2 window (band merging point), period-3 window, and period-5 window are shown. We should note that the coupling strength ϵ is so small that $\kappa \sim \epsilon$ and the dependence on κ can be replaced by the dependence on ϵ. A_{small} and A_{large} increase linearly with $\epsilon\overline{\delta h}$. As a result, the width of the tongue structure grows linearly with $\epsilon\overline{\delta h}$.

As to the growth of the amplitude of the mean-field, it has been pointed out that $\overline{\delta h} \sim \epsilon$ for the globally coupled logistic map [8,19]. In Fig. 24, $\overline{\delta h}$ in a tongue structure is plotted as a function of ϵ for several tongue structures. Although the growth of $\overline{\delta h}$ obeys a power law, there is a deviation from the linear scaling with ϵ.[8] This deviation is considered to be due to the following distinction. Whereas we have payed attention mainly to tongue structures corresponding to windows of the logistic map, in Ref. [19] such window structures in the logistic map are out of consideration. In other words, they have focused on the collective dynamics arising from completely chaotic dynamics in the logistic map.[9] Possible differences between the collective motions originating in chaos and window will be discussed in Section 10 again.

The much longer timescale of the mean-field dynamics than the dynamics of an element is an important characteristic of the collective motion, as is shown in Fig. 2, in which a frequency peak of the longer timescale arises at the frequency 0.025, whereas the shorter timescale around 0.5 is present both in the single element dynamics and in the mean-field dynamics. Asymptotic behavior of these timescales with $\epsilon \to 0$ is also an interesting problem. In Fig. 25, the frequency of the slow component is computed from the peak of the power spectrum, and is plotted as a function of

[8] We should note that it is possible to take a proper limit of $\epsilon \to 0$ in a tongue structure, sustaining the chaotic motion. For example, the edge of each tongue structure (i.e., at the crisis point) satisfies this condition. The above scaling behavior is checked by setting the parameter A to keep chaotic motion in this way.

[9] Although our analysis is based on the rescaled parameter A, although in the previous studies [8,19], a was used, the difference will not be essential for small ϵ.

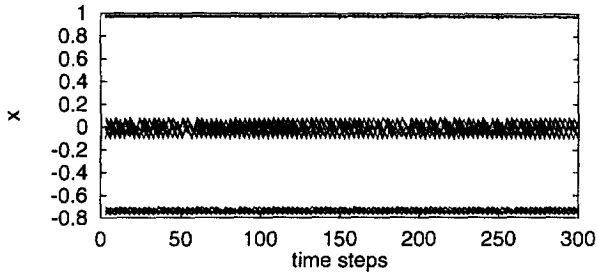

Fig. 26. One of coexisting attractors shown as a time series of elements. In this case, elements are accumulated to three bands. Time series of 100 elements out of 10^5 are plotted every third time steps. A lot of attractors exist depending on the population ratio to each band, while elements are desynchronized from each other. The parameters are $a = 1.85$, $\epsilon = 0.018$, $N = 10^5$.

ϵ for each tongue structure. [10] The shorter timescales are independent of ϵ, and are not shown in the figure. The longer timescales get even longer with $\epsilon \to 0$, as $\sim \epsilon^{\alpha}$, where the exponent α depends on the tongue structure.

9. Hysteresis, multiple attractors, and coexistence of different types of motion

Here we will study the coexistence of several attractors that can appear in the GCM. The most straightforward examples are "band splitting" mechanism of multiple attractors. Here, in the "p-band splitting", the distribution of $x_n(i)$ splits into p disconnected regions. There is no mixing of elements among disconnected regions. An example, for $p = 3$ is shown in Fig. 26. Since the number of elements at each region does not change in time, the population ratio of elements at each region gives a time invariant index for an attractor. Depending on the population ratio, there are a lot of attractors (see e.g. [14] for the case with a tent map).

In the next example, multiple attractors are found in hysteresis phenomena of collective motion, that can be observed at the edge of the tongue structure in the parameter space. In Fig. 27, the hysteresis curve of the MSD is obtained by increasing or decreasing the

[10] Here the value A for each tongue structure is chosen so that $\overline{\delta h}$ is maximized for a given ϵ, although dependence of the frequency on A is not significant.

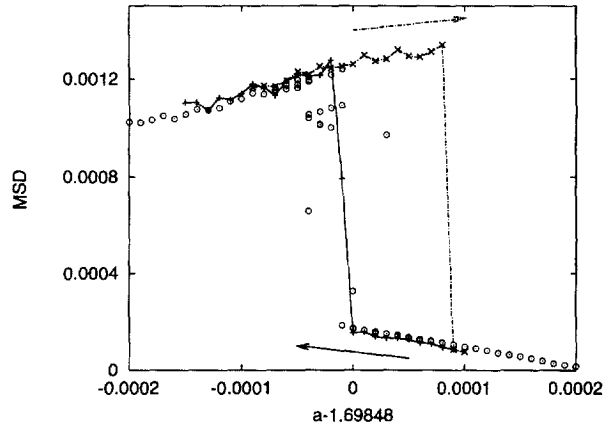

Fig. 27. Hysteresis curve observed by increasing or decreasing progressively the control parameter a while keeping the final state of a simulation at given a as the initial condition for the neighboring value $a - \delta a$ ($\times$) and $a + \delta a$ ($+$). $\epsilon = 0.008$. The MSD calculated starting from a random initial condition is also plotted ($\circ$).

control parameter a. For calculation, the final state of a simulation at the previous value of a is used for the next initial condition. Thus in $a - 1.69848 \in [0, 0.0001]$, two different collective motions exist depending on the initial condition. Hence, at least two different attractors coexist depending on the initial condition. In Fig. 28, the time series and the return map for each attractor are shown. Note that in this case there are no separated regions in contrast with the previous examples.

The third example of multiple attractors is the coexistence of two types of attractors, one with a band splitting structure (Fig. 26) and the other without a band splitting structure (Fig. 29). In an attractor with a band splitting structure, elements are accumulated in a few regions. However, in an attractor without such structure, elements spread over the whole range of x. Moreover, for the former type, there exists a lot of attractors with a different population ratio in each region, as is explained in the first example.

10. Summary and discussion

In the present paper, we have studied collective motion in the desynchronized state of the globally

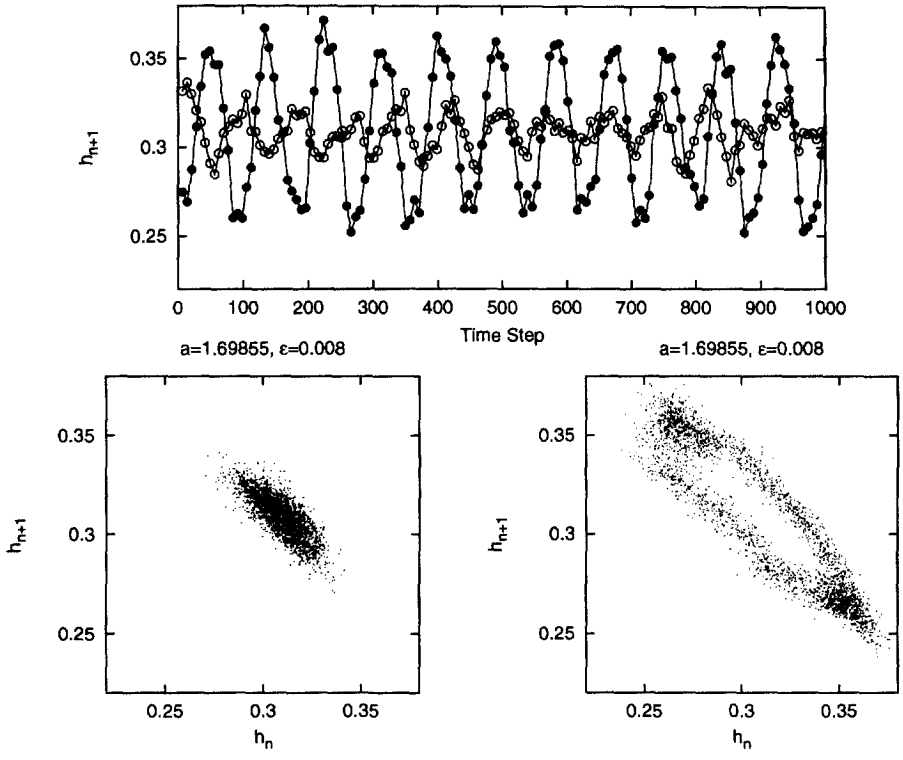

Fig. 28. Time series and return map for two attractors in Fig. 27. The parameters are $a = 1.69855$, $\epsilon = 0.008$.

coupled logistic map. It is shown that collective motion with a much longer timescale and lower dimension can emerge at a macroscopic level. The dependence of the amplitude of the collective motion on a and ϵ is studied. After some change of variables and parameters, tongue structures are clearly seen in (A, κ)-plane. Each tongue structure corresponds to a periodic window of the logistic map.

Focusing on tongue structures, we have demonstrated how such a collective motion emerges. The dynamics of the mean-field and each element form some self-consistent relationship, so that collective motion is possible. This self-consistent dynamics is formed by the following repetition: accumulation of elements into some regions leading to a change in the mean-field dynamics, which introduces a stability change of the regions, and accumulation of elements into a different region occurs, which, again... This gives internal bifurcation in elements and in time.

The bifurcation is also seen in the parameter space. Since the nature of the internal bifurcation varies with the nonlinearity parameter a in a tongue structure, the number of coexisting regions in x changes, which makes the collective motion qualitatively different. Hence, in a tongue structure, different kinds of collective motions have been observed. (A schematic figure of tongue structure is presented in Fig. 30.)

With the increase of the coupling strength ϵ, each tongue structure grows in proportion to $\epsilon \cdot \overline{\delta h}$, where $\overline{\delta h}$ is the amplitude of the mean-field variation. Hence the width of each tongue would increase with ϵ^2, if $\overline{\delta h} \propto \epsilon$ would hold. In contrast with earlier studies [8,19] supporting this linear scaling, our calculation suggests that the scaling may obey a different power law. (See also the arguments below.)

We also reported the existence of multiple attractors, each of them having a different collective motion. This

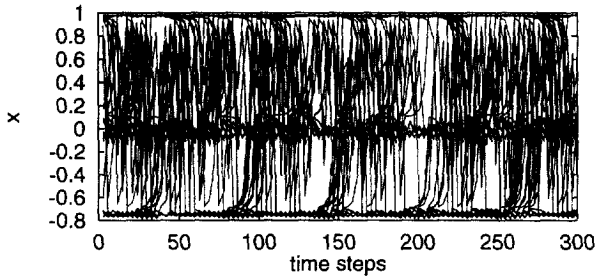

Fig. 29. Time series of elements for the same parameter in Fig. 26 starting from different initial condition. In contrast with Fig. 26, elements spread over x. The mean-field dynamics for this time series shows quasiperiodic-like motion. Time series are plotted for 100 elements at every three steps. The parameters are $a = 1.85$, $\epsilon = 0.018$, $N = 10^5$.

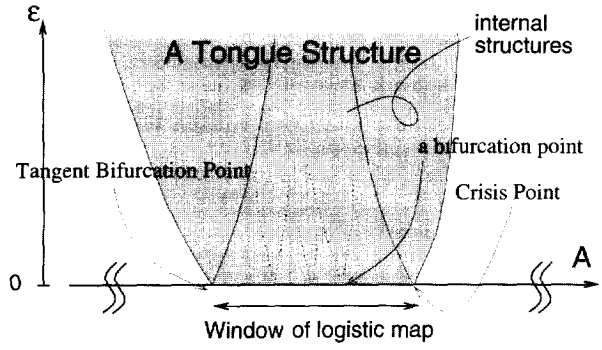

Fig. 30. Schematic diagram of a tongue bifurcation structure. Regions that grow from a bifurcation point of the logistic map constitute a tongue structure. See Section 7.

means that there can be a nonunique self-consistent dynamics between microscopic and macroscopic motion. Since the average mean-field is clearly different for each attractor, the effective nonlinearity parameter A is different for each attractor. In this way, the different attractors are distinguishable clearly in the (A, κ)-plane.

The tongue structure is based on the underlying windows of the single logistic map. Windows exist in any neighborhood of the parameter space of the single logistic map. The tongue structures of the GCM expands with the increase of ϵ from each window of the single logistic map at $\epsilon = 0$. So, the tongue structure is expected to occupy a relatively large region in the parameter space. This is one of the reasons why we have focused our attention on the collective behavior in the tongue structures. Still, we have to note that there is a positive measure in the parameter space of the logistic map, corresponding to chaos. Hence, at least for small coupling in the GCM, there are parameters with a positive measure which do not belong to any tongue structure. Indeed, we have observed that the amplitude of the mean-field variation drops less than to 0.1 (see Fig. 10), at the parameter where the tongue structure disappears. Although no clear structure in the return map is detected there, this motion again has some hidden coherence and is distinguishable from noise.

Analytical estimate of the mean-field dynamics by Ershov et al. [19] is based on singularities of distributions. Only the fluctuation due to singularities of the probability distribution function is taken into account by neglecting regular parts of the probability distribution function. Our result may imply that the regular parts, which are relevant to the windows of local mapping, should be taken into account for the collective motion. Careful analysis of both the regular and singular parts may be required. This might be the reason why the scaling of δh is different from Ershov's estimation. As we have noted above, however, Ershov's analysis is applied to the collective dynamics originated in the chaotic regime of the single logistic map. We need further study in the chaotic regime to clarify the mechanism of the collective dynamics there, and to characterize the high-dimensional chaos.

Even if the elements are completely desynchronized from each other, for some case, some kind of predictability may emerge in the macroscopic variables, although all the Lyapunov exponents are positive. It might be also important to study how the predictability of the collective motion reflect on N-dimensional phase space structure or on microscopic quantities, such as the Lyapunov spectrum. With such study, the mechanism for the collective motion must be clearly distinguishable from the self-organization mechanism [26] or the slaving principle [27]. Although we have presented a heuristic way to extract such self-consistent dynamics in the present paper, it is hoped that a systematic method

to characterize collective motion will be developed in future. [11]

Acknowledgements

Acknowledgment is due to T. Chawanya, S. Morita, and S. Sasa for valuable discussions of this work. One of the authors (TS) also thanks E. van Nimwegen and J.P. Crutchfield for fruitful discussions and valuable comments. The authors also gratefully acknowledge S.V. Ershov for his suggestion to improve the manuscript, and R. Merks for careful reading of the manuscript. A part of the numerical calculation was carried out at Yukawa Institute Computer Facility. This work is partially supported by Grant-in-Aids for Scientific Research from the Ministry of Education, Science, and Culture of Japan.

References

[1] S. Watanabe, S.H. Strogatz, Constants of motion for superconducting Josephson arrays, Physica D 74 (1994) 197–253; and references therein.

[2] C. Bracikowski, R. Roy, Chaos in a multimode solid-state laser system, Chaos 1 (1991) 49; F. T. Arecchi, Rate processes in nonlinear optical dynamics with many attractors, Chaos 1 (1991) 357.

[3] Ad Aertsen, M. Erb, G. Plam, Dynamics of functional coupling in the cerebral cortex: an attempt at a model-based interpretation, Physica D 75 (1994) 103–128; and references therein.

[4] E.P. Ko, T. Yomo, I. Urabe, Dynamics clustering of bacterial population, Physica D 75 (1994) 81–88; K. Kaneko, T. Yomo, Cell division, differentiation and dynamic clustering, Physica D 75 (1994) 89–102.

[5] P.J. Godin, T.G. Buchman, Uncoupling of biological oscillators: A complementary hypothesis concerning the pathogenesis of multiple organ dysfunction syndrome, Crit. Care. Med. 24 (1996) 1107–1116; T.G. Buchman, Physiological stability and physiologic state, J. Trauma 41 (1996) 599–605.

[6] K. Kaneko, Clustering, coding, switching, hierarchical ordering, and control in a network of chaotic elements, Physica D 41 (1990) 137–172.

[7] K. Kaneko, Globally coupled chaos violates the law of large numbers, Phys. Rev. Lett. 65 (1990) 1391.

[8] K. Kaneko, Mean field fluctuation of a networks of chaotic elements, Physica D 55 (1992) 368–384.

[9] G. Perez, H.A. Cerdeira, Instabilities and nonstatistical behavior in globally coupled systems, Phys. Rev. A 46 (1992) 7492.

[10] H. Chaté, P. Manneville, Collective behaviors in spatially extended systems with local interactions and synchronous updating, Progr. Theoret. Phys. 87 (1992) 1.

[11] G. Perez, S. Sinha, H.A. Cerdeira, Order in the turbulent phase of globally coupled maps, Physica D 63 (1993) 341–349.

[12] A.S. Pikovsky, J. Kurths, Do globally coupled maps really violate the law of large numbers?, Phys. Rev. Lett. 72 (1994) 1644; A.S. Pikovsky, J. Kurths, Collective behavior in ensembles of globally coupled maps, Physica D 76 (1994) 411–419.

[13] W. Just, Bifurcations in globally coupled map lattices, J. Stat. Phys. 79 (1995) 429.

[14] K. Kaneko, Remarks on the mean-field dynamics of networks of chaotic elements, Physica D 86 (1995) 158–170.

[15] S.V. Ershov, A.B. Potapov, On mean field fluctuations in globally coupled maps, Physica D 86 (1995) 532–558.

[16] S. Morita, Bifurcation in globally coupled chaotic maps, Phys. Lett. A 211 (1996) 258–264.

[17] H. Chaté, A. Lemaitre, Ph. Marcq, P. Manneville, Non-trivial collective behavior in extensively-chaotic dynamical systems: an update, Physica A 224 (1996) 447–457.

[18] T. Shibata, K. Kaneko, Heterogeneity induced order in globally coupled chaotic systems, Europhys. Lett. 38 (6) (1997) 417–422.

[19] S.V. Ershov, A.B. Potapov, On mean field fluctuations in globally coupled logistic-type maps, Physica D 106 (1997) 9–38.

[20] N. Nakagawa, T. Komatsu, Collective motion occurs inevitably in a class of populations of globally coupled chaotic elements, Phys. Rev. E 57 (1998) 1570.

[21] T. Chawanya, S. Morita, On the bifurcation structure of the mean-field fluctuation in the globally coupled tent map systems, Physica D 116 (1998) 44.

[22] K. Kaneko, Period-doubling of kink-antikink patterns, quasi-periodicity in antiferro-like structures and spatial intermittency in coupled logistic lattice – toward a prelude to a "field theory of chaos" –, Prog. Theor. Phys. 72 (1984) 480; Pattern dynamics in spatiotemporal chaos, Physica D 34 (1989) 1; in: K. Kawasaki, A. Onuki, M. Suzuki (Eds.), Simulating Physics with Coupled Map Lattice, Formation, Dynamics, and Statistics of Patterns, World Scientific. Singapore, 1990; in: K. Kaneko (Ed.), Theory and Applications of Coupled Map Lattices, Wiley, New York, 1993.

[23] N. Nakagawa, Y. Kuramoto, From collective oscillations to collective chaos in a globally coupled oscillator system, Physica D 75 (1994) 74–80.

[24] M. Chabanol, V. Hakim, W. Rappel, Collective chaos and noise in the globally coupled complex Ginzburg–Landau equation, Physica D 103 (1997) 273–293.

[11] So far, we have no conventional tool for detecting the lower-dimensional collective signals out of high-dimensional signals. In [28], we will develop a tool to distinguish and characterize several collective dynamics in GCM.

[25] P. Grassberger, I. Procaccia, Characterization of strange attractors, Phys. Rev. Lett. 50 (1983) 346; Measuring the strangeness of strange attractors, Physica D 9 (1983) 189.
[26] G. Nicolis, I. Prigogine, Self-Organization in Non-equilibrium Systems, Wiley, New York, 1977.
[27] H. Haken, Synergetics, Springer, Berlin, 1976.
[28] T. Shibata, K. Kaneko, Collective Chaos, Phys. Rev. Lett. (1998), submitted; preprint xxx.lanl.gov chao-dyn/9805009.